



Article

The Electric Field Detector on Board the China Seismo Electromagnetic Satellite—In-Orbit Results and Validation

Piero Diego ^{1,*}, Jianping Huang ^{2,*}, Mirko Piersanti ³, Davide Badoni ³, Zhima Zeren ², Rui Yan ², Gianmaria Rebutini ^{3,4}, Roberto Ammendola ³, Maurizio Candidi ¹, Yi-Bing Guan ⁵, Jungang Lei ⁶, Giuseppe Masciantonio ³, Igor Bertello ¹, Cristian De Santis ³, Pietro Ubertini ¹ and Xuhui Shen ² and Piergiorgio Picozza ^{3,4}

- ¹ INAF-Istituto di Astrofisica e Planetologia Spaziali, Rome 00133, Italy; maurizio.candidi@inaf.it (M.C.); igor.bertello@inaf.it (I.B.); pietro.ubertini@inaf.it (P.U.)
- ² National Institute of Natural Hazards, Ministry of Emergency Management of China, Beijing 100085, China; zerenzhima@ninhm.ac.cn (Z.Z.); yanxiaoxiao_best@163.com (R.Y.); Shenxh@seis.ac.cn (X.S.)
- ³ INFN—Sezione di Roma “Tor Vergata”, Rome 00133, Italy; mirko.piersanti@roma2.infn.it (M.P.); davide.badoni@roma2.infn.it (D.B.); gianmaria.rebutini@roma2.infn.it (G.R.); roberto.ammendola@roma2.infn.it (R.A.); giuseppe.masciantonio@roma2.infn.it (G.M.); cristian.desantis@roma2.infn.it (C.D.S.); piergiorgio.picozza@roma2.infn.it (P.P.)
- ⁴ Physics Department, University of Rome “Tor Vergata”, Rome 00133, Italy
- ⁵ National Space Science Center-CAS, Beijing 100190, China; gyb@nssc.ac.cn
- ⁶ Lanzhou Institute of Physics, Lanzhou 730000, China; lei7412@163.com (J.L.)
- * Correspondence: piero.diego@inaf.it (P.D.); xhhjp@126.com (J.H.)

Abstract: The aim of this work is to validate the China Seismo-Electromagnetic Satellite 01 (CSES-01) Electric Field Detector (EFD) measurements through the analysis of the instrument response to various inputs: (a) geomagnetic field variations, (b) plasma density depletions, and (c) electromagnetic signals from natural and artificial sources such as Schumann resonance and VLF (Very Low Frequency) antennas. The knowledge of the geomagnetic induced electric field $v_s \times B$ (where v_s is the satellite speed and B and the local magnetic field), and the plasma variations effect, described by the Orbit Motion Limited (OML) theory, are key parameters to determine the expected theoretical values of the EFD sensors potentials data. Based on the CSES on-board measurements of plasma parameters and geomagnetic field, a direct quantitative validation is presented. In addition, the electromagnetic signals detection capability is checked but only qualitatively confirmed, since the ionospheric complexity does not allow an accurate theoretical computation of waves modulation. The quantitative comparison highlights the very good agreement between observed and theoretical potentials values during average condition. Conversely, in case of strong electric fields, the OML theory shows partial inability in reproducing the actual space plasma conditions resulting in a reduced theoretical values reliability. Finally, both natural and artificial electromagnetic signals are satisfactorily identified showing a reliable sensitivity in different frequency bands.

Keywords: electric field instrument; low earth orbiting satellite; plasma physics



Citation: Diego, P.; Huang, J.; Piersanti, M.; Badoni, D.; Zeren, Z.; Yan, R.; Rebutini, G.; Ammendola, R.; Candidi, M.; Guan, Y.-B.; et al. The Electric Field Detector on Board the China Seismo Electromagnetic Satellite—In-Orbit Results and Validation. *Instruments* **2021**, *5*, 1. <https://dx.doi.org/10.3390/instruments5010001>

Received: 19 November 2020

Accepted: 21 December 2020

Published: 24 December 2020

Publisher’s Note: MDPI stays neutral with regard to jurisdictional claims in published maps and institutional affiliations.



Copyright: © 2020 by the authors. Licensee MDPI, Basel, Switzerland. This article is an open access article distributed under the terms and conditions of the Creative Commons Attribution (CC BY) license (<https://creativecommons.org/licenses/by/4.0/>).

1. Introduction

The China Seismo-Electromagnetic Satellite 01 (CSES-01) was launched on 2 February 2018 into a sun-synchronous, polar and Low Earth Orbit (LEO) at an altitude of 507 km with an inclination of $\sim 97^\circ$ and a period of ~ 95 min to inspect natural electromagnetic phenomena possibly related to earthquakes [1]. The Electric Field Detector (EFD) measures the electric potentials of four spherical sensors with reference to spacecraft (S/C) potential, located at the tip of four 4.5-m long booms, and derives the electric field in the frequency range between about DC and 3.5 MHz [2]. Its working principle is the active double-probe technique, so that the electric field (E) components are obtained as the difference between the probes voltages divided by the distance d between the various probes pairs. It is worth

reminding that E contains the spurious effect induced by the satellite motion in the Earth's magnetic field which has to be removed [3].

Figure 1 shows the EFD sensors position in the satellite orbit system. X_s, Y_s and Z_s are defined as: X_s is the flight direction, Z_s is directed from the satellite to the Earth, and Y_s completes the orthogonal right-handed system. It can be easily seen that, approximately, probe A lays in the $X_s - Y_s$ plane, and is directed opposite to Y_s , probe B lays in the $Z_s - X_s$ plane, directed at 45° between the $-X_s$ and $-Z_s$ axes, and probes C and D are deployed in the $X_s - Z_s$ and $Z_s - Y_s$ planes, respectively [2]. The distances among the 4 probes are reported in Table 1.

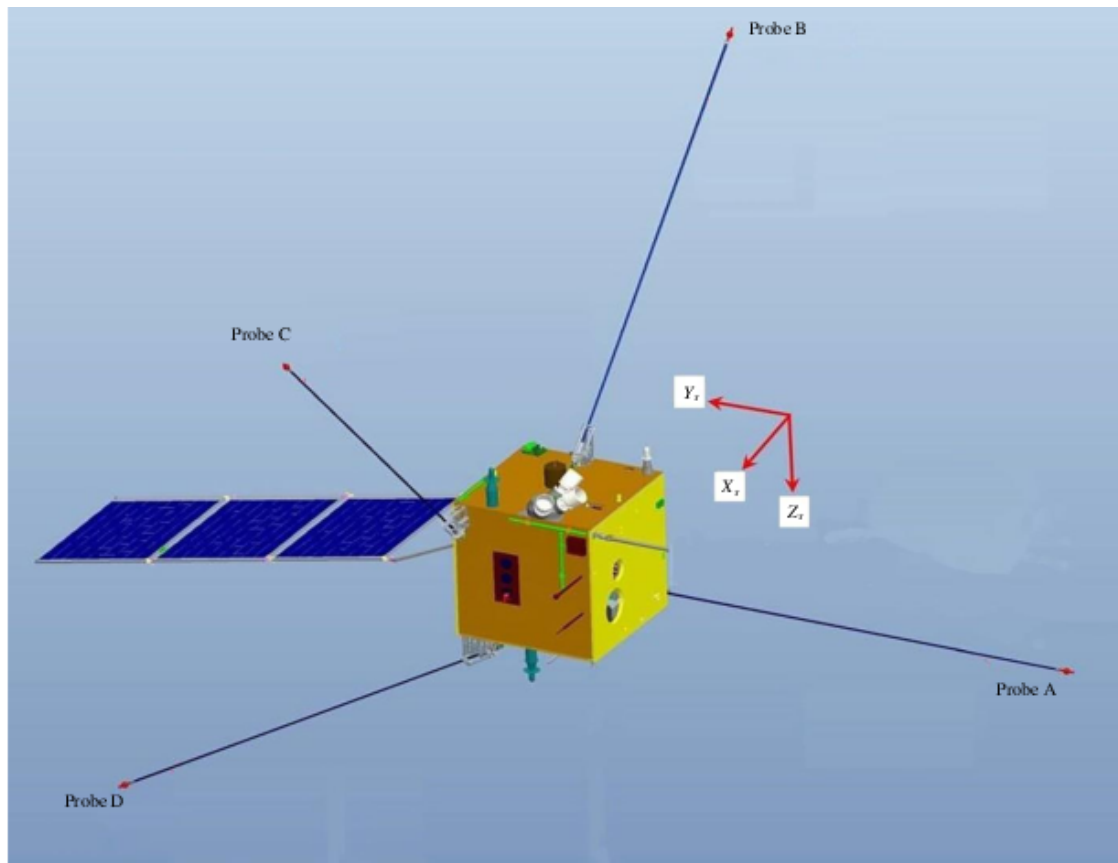


Figure 1. Configuration of Electric Field Detector (EFD) on-board the China Seismo-Electromagnetic Satellite (CSSES). The reference frame (X_s, Y_s and Z_s ; X_s is directed along the satellite motion) is the satellite orbit system (see explanation in the text). Adapted from Huang et al. [2].

Table 1. Distance between probes. Adapted from Huang et al. [2].

	Probe b	Probe c	Probe d
Probe a	7315 mm	8329 mm	9566 mm
Probe b	-	7647 mm	9298 mm
Probe c	-	-	9394 mm

The electric field components in the S/C reference frame are evaluated along the directions defined by the various sensors pairs, from the voltage differences:

1. $V_1 = V_a - V_b$,
2. $V_2 = V_c - V_d$,
3. $V_3 = V_a - V_d$.

where V_a, V_b, V_c, V_d are the probes potentials. The electric field components are initially computed in the satellite coordinate system and then rotated into the geographical reference frame (X, Y and Z) (Huang et al. [2]).

The main goal of the EFD is to measure the ionospheric E field over a broad frequency band with high sampling rates. The frequency bands (ULF, ELF, VLF and HF), with their principal characteristics [2], are reported in Table 2.

Table 2. Characteristics of the EFD for the different frequency bands [2].

Band	Sampling Frequency- f_s (Hz)	Resolution (μVm^{-1})	Sensitivity ($\mu\text{Vm}^{-1}\text{Hz}^{-1/2}$)	Dynamical Range (dB)	Spectral Frequency Resolution (Hz)	Spectra Time Resolution (s)
ULF (Waveform)	125	1	0.1	120	-	-
ELF (Waveform)	5×10^3	1	0.1	120	-	-
VLF (Spectrum-Survey)	50×10^3	-	0.05	96	$f_s/2048$	2.048
VLF (Waveform-Burst)	50×10^3	-	0.05	96	-	-
HF (Spectrum)	10×10^6	-	0.1	96	$f_s/2048$	2.048

The EFD data acquisition is performed in two observation modes (survey and burst) as shown in Table 2. The burst mode is activated over specific regions to increase the data collection. Such operational mode occur for about 2 h/day. In particular, in the ULF (Ultra Low Frequency) and ELF (Extremely Low Frequency) bands, the EFD collects the waveform electric field data along the whole orbit in survey mode. In the VLF (Very Low Frequency) band, the survey mode continuously provides the power spectral density (PSD), while waveform data is provided only in burst mode. Finally, at the HF band, EFD works only in survey-mode, producing PSD values.

In this paper, the electric field data from the CSES EFD measurements have been analyzed together with two other on-board instruments in order to validate the EFD response to environmental variations. One instrument is the Langmuir probe (LAP) which measures in-situ the ionospheric plasma parameters with a sampling period of 3 s in survey-mode, and 1.5 s in burst mode [4]. The second instrument is the high precision magnetometer (HPM) which measures the geomagnetic field from about DC to 15 Hz providing both vector and scalar values [5]. In particular, magnetic field and plasma data have been used to compute the expected EFD values according to the Orbit Motion Limited theory ([6] and reference therein) and the impact of the magnetic field on the sensors wiring ($v \times B$ effect). In addition, both natural and anthropogenic signals with well known frequency characteristics have been used to check the EFD capability in detecting electromagnetic oscillations. For these analyses, we have chosen a nightside orbit to reduce the additional noise induced by the sunlight, thus to better evaluate the sensitivity of the instrument.

2. Comparison between Expected and Measured Electric Field Values.

The sensors potential (also called “floating potential” V_f) used to compute the Electric field, is the equilibrium point among currents collected by the probe ([2,3,7]). The equations for the currents reported in Diego et al. [3] clearly show their dependence on the plasma

density and temperature, except for the photo-electrons current that depends on probe materials and sun light exposure (i.e., it is equal to zero in the nightside of the S/C orbit). In addition, the bias current is directly injected by the EFD instrument electronics to minimize the contact impedance between probe and plasma. Since the plasma parameters are available as measured by the Langmuir probes (LAP) on-board the satellite, and both photo-electrons and bias currents are known (zero and 500 nA respectively), it is possible to compute the expected theoretical probe potentials values (called V_{theo} hereafter) with its sampling rate (i.e., about 0.3 Hz) [4].

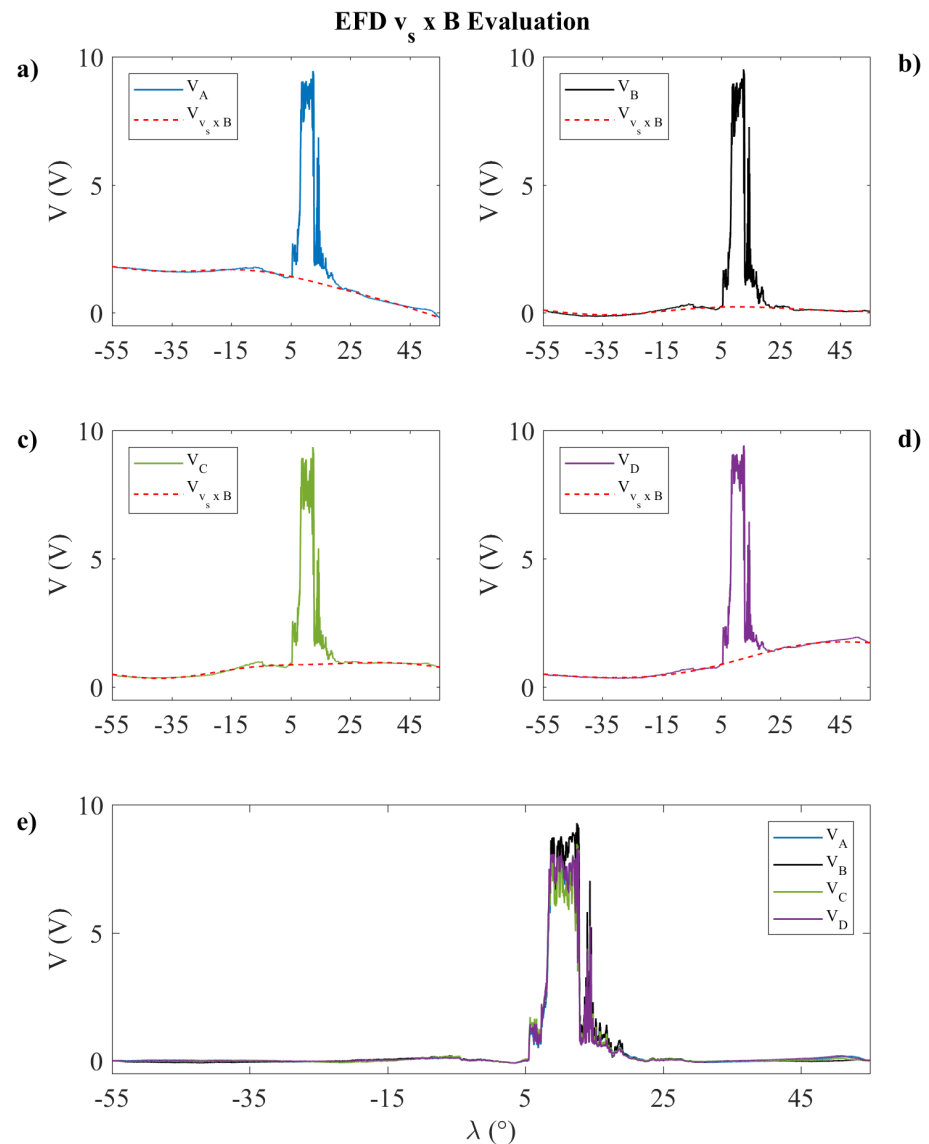


Figure 2. Upper panels (a, b, c, and d) show the probes potentials variations due to the $v_s \times B$ geomagnetic field effect. The red dotted line represents the computed $v_s \times B$. The lower panel (e) shows the potentials when the computed $v_s \times B$ is subtracted from the measured value vs. the geographic latitudes λ .

The probe potentials are strongly dependent on the $v_s \times B$ induced electric field (v_s and B are the spacecraft speed and the local magnetic field, respectively) that produces a low frequency modulation on EFD measurements due to the slow changes of geomagnetic

field along the satellite orbit. Since the booms attitudes, with respect to the magnetic field, are different, each probe has a different and variable bias that must be carefully computed along the orbit by using magnetic field measurements (e.g., High Precision Magnetometer (HPM) on-board CSES) and the housekeeping data for velocity and attitude. In the following subsections, the expected EFD potentials values have been inferred from the plasma and fields variations. The results are compared to show the EFD data reliability under both quiet and perturbed conditions. In order to easily compare the expected theoretical values with the instrumental measurements, we selected an orbit characterized by both quiet and perturbed conditions. We define as perturbed, a part of orbit where the spacecraft experiences the occurrence of a strong electric field which can alter the electrons collection by the probes (i.e., OML theory is no longer valid in describing the current collected on the probe's surface). The threshold value to identify such strong perturbation has been computed by comparing the electrons thermal energy with that induced by the electric field:

$$\frac{3}{2}k_b \cdot T_e = q \cdot E_s \cdot d, \quad (1)$$

where k_b is the Boltzmann constant, T_e is the electron temperature, q is the electron charge, d is the average probe distance, and E_s is the corresponding threshold value electric field that balances Equation (1). Therefore, using the typical value of the electron temperature at CSES altitude (~ 2000 K average value as identified in Diego et al. [3] by using IRI model) and $d \sim 8$ m, the thermal effects result to be dominant for electric field lower than $E_s \sim 40$ mV/m. Thus, we considered as unperturbed the case with electric field lower than the threshold value of 4 mV/m (corresponding to $\sim 10\%$ of E_s).

On the other hand, we can define the perturbed cases when the electric field rises up to few tens of mV/m so that the electrons flow starts to depend on the forcing field, until the electrons collection is completely dominated by the electric effect for $E_s > 100$ mV/m. Figure 2 shows the CSES-01 night side orbit n. 029301 (14 August 2018), in which both the quiet and perturbed conditions are encountered: the perturbation can be easily identified as a sharp V_f enhancement at $\sim 10^\circ$ of latitude. The strong potential variation is due to the occurrence of a plasma bubble as described by [8]. Finally, the comparison between measured and computed values is performed on the down-sampled EFD data (reduced at 0.3Hz by using a linear interpolation method).

2.1. Quiet Condition

The $v_s \times B$ is a low frequency contribution to the electric field measurements. The upper panels (labelled with letters a to d) in Figure 2, clearly show that the various probes potentials have different levels and shapes (clearly visible outside the perturbation that occurs between $\sim 5^\circ$ and $\sim 20^\circ$ latitudes). The red dotted lines represent the computed $v_s \times B$ that perfectly fits the signals, except for the perturbed sector. In Figure 2e the $v_s \times B$ has been subtracted from the four V_f time series, thus showing that these have almost the same trend in the quiet sectors. The upper panel of Figure 3 shows the amplitude of the electric field components for both quiet ($\lambda < 5^\circ$ and $\lambda > 20^\circ$) and perturbed locations ($5^\circ < \lambda < 20^\circ$). The lower panel shows the four V_f along with the V_{theo} (green line) derived from OML equations. Since the OML theory does not take into account perturbing fields, V_{theo} can fit V_f only if the plasma parameters inputs (density and temperature) are reliable. In order to verify the possible agreement between expected and measured EFD potentials, we have computed their differences for the quiet period, as shown in Figure 4. The average of each distribution is lower than 0.3 mV and the standard deviation (SD) lower than 5 mV, confirming a very good agreement between V_{theo} and each probe potential.

In addition, to better understand the origin of the distributions width in Figure 4, we have performed the cross correlation among various probes pairs by using data collected at 5 kHz (i.e., the sample rate of the lower band). In fact, assuming the plasma N_e and T_e to be constant within distance scales comparable with the sensors distances (see Table 1) all the sensors should have the same V_f , once the $v_s \times B$ effect is removed. Any differences among the sensors V_f should be due to plasma oscillations induced by electromagnetic phenomena.

According to such hypothesis, the cross correlation among various sensors is checked to identify the oscillation coherence. The zero-lag peaks in Figure 5 allow to address the SD amplitude to V_f variation such as electromagnetic oscillations superimposed to the average values that are very close to the expected ones V_{theo} .

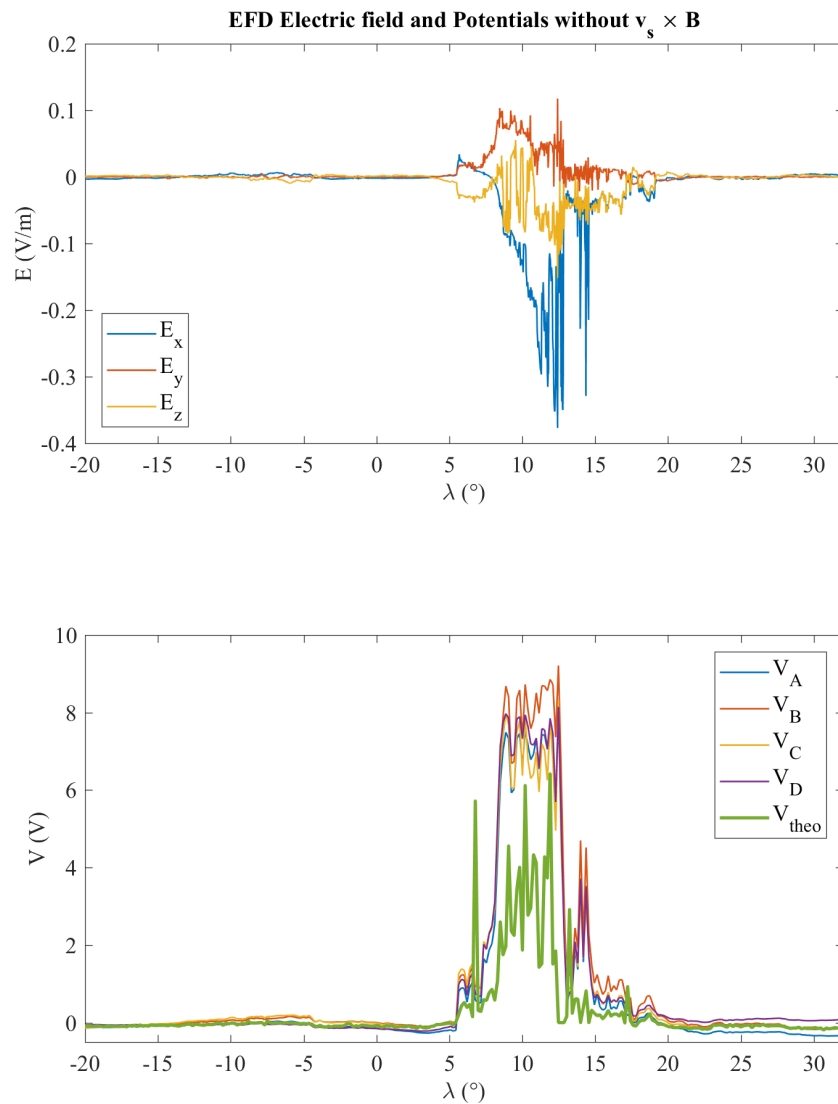


Figure 3. The upper panel shows the three component of the electric field on the nightside low latitude part of the CSES orbit n. 02930. The lower panel displays the four probes potentials along with the computed V_{theo} (green line). λ is the geographic latitude.

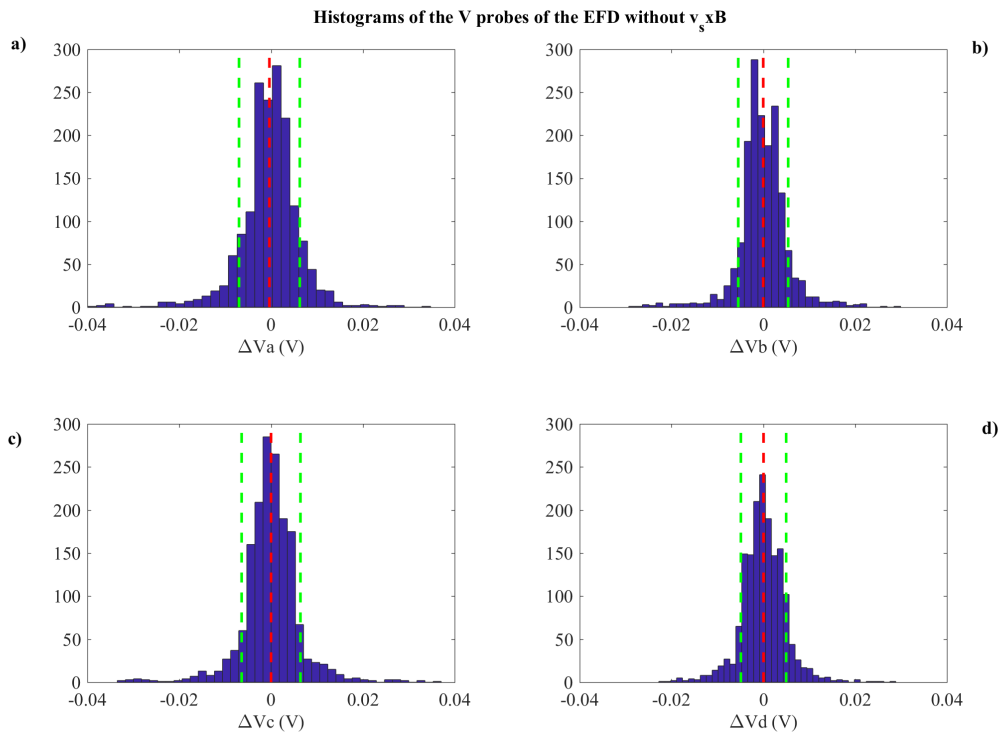


Figure 4. Distributions of the differences between probe potential V_i and the expected value V_{theo} for the various probes in the quiet period. Panel labels (a, b, c, and d) indicate the probe used to compute the difference with the theoretical value. Red vertical dashed lines indicate the mean value. Green vertical dashed lines indicate values at \pm one SD.

2.2. Perturbed Condition

The plasma depletion encountered at low latitude in Figure 2 is detected by both Langmuir probes (LAP) and EFD instruments of CSES. The plasma density from LAP measurements are abruptly reduced by about two orders of magnitude, that is, from about 10^{10} m^{-3} down to 10^8 m^{-3} or lower values in the central part of the plasma bubble and reference therein [8]. The EFD sensors reach high positive values due to the increasing ratio between the injected bias (fixed at 500 nA) and the collected plasma currents. In this condition, the differences between V_f and V_{theo} increase up to few Volts and the measured V_f are, on average, about 3 times higher with respect to the V_{theo} . This effect depends on the induced unbalancing in ions and electrons collection on the probes, due to the electric field effect on the electrons flow direction. In fact, according to the OML theory, the electrons flow should be isotropic, thus the spherical sensors collect electrons on all their surface (i.e., $4\pi \cdot r^2$). On the other hand, when a strong electric field is present, the OML is no longer valid in describing the electrons collection because their flow becomes more directional. In the case of very strong fields ($>100 \text{ mV/m}$) the flow is completely dominated by the electric field direction, and the collecting surface on the probes is reduced up to a factor four as for the case of ion collecting surface that, in OML, is considered to be simply the cross section of the sphere under a unidirectional particles flow (i.e., $\pi \cdot r^2$).

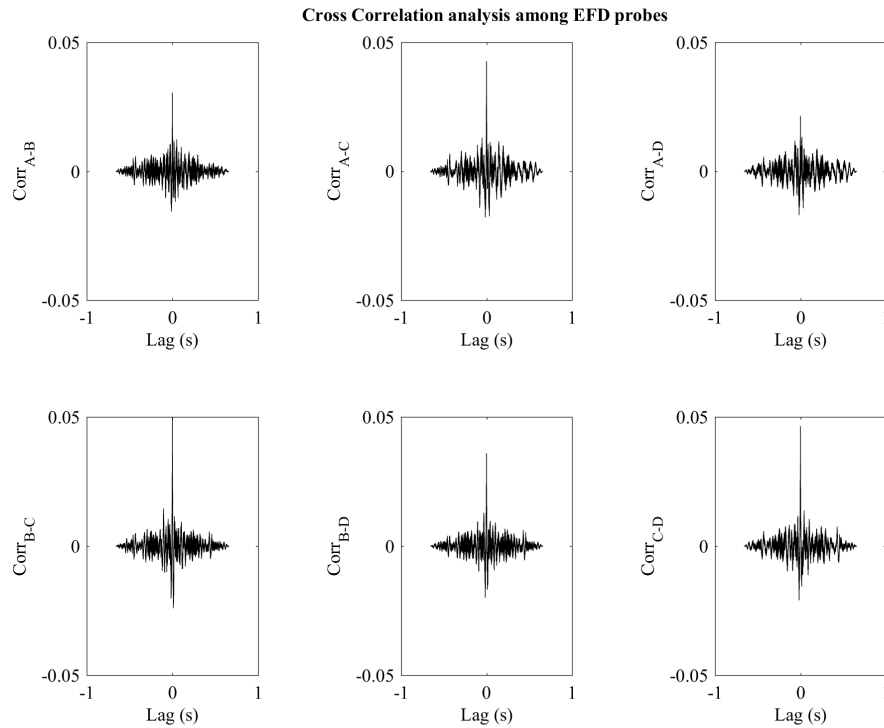


Figure 5. Cross correlation between six couples of probes potentials. The zero lag value represents the null shifting between signals variations.

The EFD sensors potentials naturally change to balance the variation in particle fluxes to obtain the total current, flowing on it, to be equal to zero (according to Kirchhoff's nodal rule). Thus, we can still consider EFD data as absolutely reliable. Conversely, the LAP plasma parameters are computed with OML equations, therefore the electrons density is underestimated due to the collecting surface, which is not easy to model and calculate. The reduction of the electrons flow on the sensors regions parallel to the electric field, result in a factor of ~ 2 decrease in the current collection (in case of several tens of mV/m) to ~ 4 (for $E_s > \text{hundred mV/m}$) as shown in the distributions of Figure 6. Note that the distributions are not strictly Gaussian due to the lower number of samples used and to the variable electric field occurred. Nevertheless, we used the SD to briefly evaluate the range of induced discrepancy. The measured values are qualitatively in agreement with the expected V_{theo} since the ratio between V_f and V_{theo} is on average ~ 3 inside the plasma bubble.

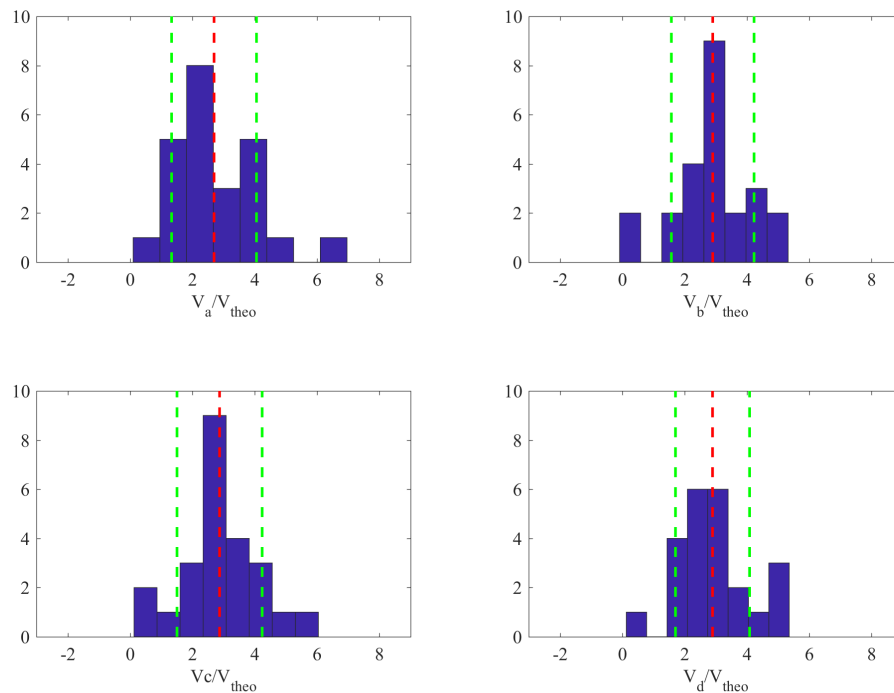


Figure 6. Distributions of the ratios between probe potential V_i and the expected value $V_{i,theo}$ inside the plasma bubble for the CSES orbit n. 029301. Red vertical dashed lines indicate the mean value. Green vertical dashed lines indicate the range at one standard deviation.

3. EFD Capability in Observing Natural/Artificial Electromagnetic Signals

The EFD on-board CSES has been conceived to detect electromagnetic signals related with various physical phenomena. In fact, the occurrence of anomalous signals with respect to those induced by the Sun-Earth interaction e.g., References [9–13] or by man-made electromagnetic waves (such as VLF transmitters, radio waves, and so on) and reference therein [14] can represent a characteristic marker useful to develop lithosphere-ionosphere-magnetosphere coupling models e.g., References [15,16]. Moreover, the sporadic modulation of well known signals can be of great interest to evaluate changes in the ionospheric electromagnetic propagation properties. For this reason, the EFD capability to detect both natural and anthropogenic signals is extremely important. In the following sub-sections, a sample of signals detection capability, for the above mentioned different kinds of e.m. waves, is given.

3.1. Schumann Resonance

The investigation of the main phenomena taking place in the ionospheric cavity (i.e., electromagnetic sources, properties of the medium, and boundary conditions) has been done via the Schumann resonance concept [17]. The Earth can be considered as a conducting sphere, covered by the neutral atmosphere (dielectric layer). In the ionosphere, where the conductivity is significant, any atmospheric electric discharge (such as transient luminous event-TLE-, lightning, elves, and so on) can produce broadband electromagnetic waves propagating between ground and the ionosphere. The electromagnetic modes supported in such ionospheric cavity are both longitudinal and transverse. The former mode is characterized by global and almost horizontal propagation, while the latter corresponds to local and almost vertical propagation between the Earth's surface and the ionosphere [17]. In general, lightnings produce standing waves whose wavelengths are directly linked to the radius of the cavity. Their occurrence peaks over the continents (especially at low

latitudes). Such phenomenon is called Schumann resonance and presents the following eigen-frequencies:

$$\omega_n = \frac{c \cdot (n(n+1))^{1/2}}{2\pi \cdot R_E}, \quad (2)$$

where c is the speed of light, R_E is the Earth's radius, and $n = 1, 2, 3, 4 \dots$ are the relative eigen-modes [18]. The first four eigen-modes are, approximately, 7.8, 14.3, 20.8 and 33.3 Hz and reference therein [17].

In order to identify possible signatures of the Schumann resonance in the EFD observations, the perpendicular electric field component (E_{\perp}) has been evaluated by rotating the EFD data into the mean-field-aligned coordinate system [9] calculated using the CHAOS-6 model [19] as the reference magnetic field along the CSES orbit. A spectrogram of E_{\perp} , recorded on 10 August 2018 (nightside of the CSES orbit 2879), is reported in Figure 7. The Schumann resonances were identified in Figure 7 as the horizontal black dashed lines with peaks at about 7.8, and 15.0 Hz. As for the C/NOFS satellite [20] the resonances were typically observed during every satellites orbit. Anyway, it is worth noticing that they have been typically observed during nighttime conditions, suggesting that the resonant wave energy cannot efficiently penetrate the more dense daytime plasma [20]. In order to estimate wave propagation conditions in the cavity, we can compute the Q-factor, which is defined as the ratio between the accumulated field power and the power lost in the oscillation period. Such Q-factor gives information about the ELF wave attenuation produced by the electric field instrument measurements [17]. Following the Simoes et al. [20] approach, we can evaluate Q for each Schumann peak detected as:

$$Q_n = f_n / \Delta f_n, \quad (3)$$

where Δf_n is the full width at half maximum of n-th peak n and f_n is the frequency of the relative peak. We obtained the following Q values: $Q(7.8 \text{ Hz}) = 7.3$; $Q(15 \text{ Hz}) = 3.2$. These values are consistent with those of both ground observations [21] and previous satellite measurements [20].

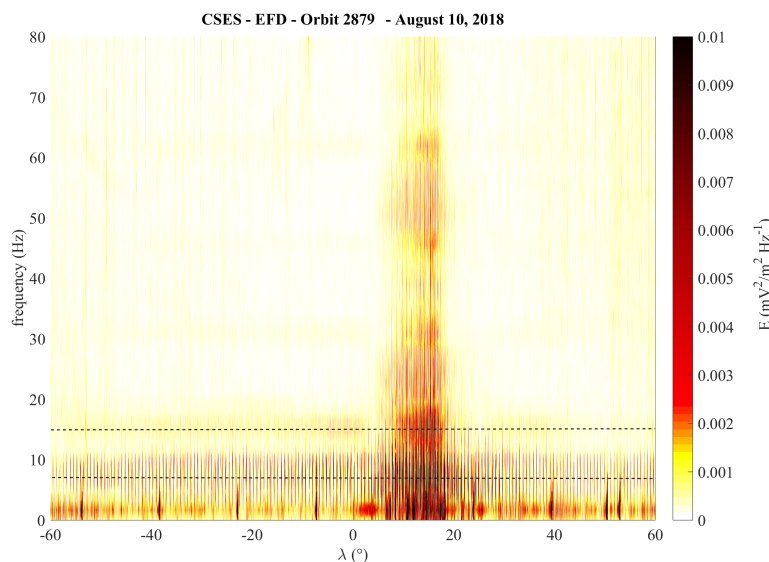


Figure 7. Spectrogram of electric field data in the frequency range between DC to 80 Hz for a nightside semi-orbit of the CSES satellite. Geographic latitude is given on the X-axis. The horizontal black dashed lines with peaks at about 7.8, and 15.0 Hz represents the detected Schumann resonances.

3.2. VLF Radio-Waves

Long-distance communication and submarines navigation are principally based on ground-based VLF transmitters, whose frequencies are in the range 10–30 kHz. It is well known that most of the ground VLF transmitters are located in a wide range of L-shell, emitting radio signals with either an impulsive modulation or a 10-s period, and are characterized by amplitudes between some kW and 1 MW and see Reference therein [22]. Because of the action of the ionospheric D region (i.e., due to collisions), the VLF radio wave energy can be partially lost. Anyway, the remaining VLF signal can further propagate through the ionosphere into the inner magnetosphere as a ducted whistler [23]. Past space missions clearly observed VLF radio waves in both the ionosphere and the inner magnetosphere e.g., References [14,24,25]. Parrot et al. [26] and Záhlava et al. [27], using observations from DEMETER satellite made an accurate analysis of both the spatial and temporal distribution of the electromagnetic field excited by the VLF transmitters. Shen et al. [28] found VLF radio wave propagation anomalies associated to changes in the environmental electric field during earthquake time both from ground-based VLF radio receiver network and DEMETER satellite.

An example of CSES-01 detection of VLF ground transmitter signals is reported in Figure 8, which shows the spectrogram of the electric field components recorded on 2 February 2019 between 18:27 UT and 19:02 UT close to the 19.8 kHz NWC transmitter (North West Cape, Exmouth, Western Australia $\lambda = 21.81^\circ$ S, $\phi = 114.165^\circ$ E). The transmitter frequency clearly appears at 19.8 kHz in the spectrogram at all the electric field components. A huge increase in the power is recorded above the emitter, as expected for ionospheric heating induced by the VLF transmitter and quite well observed by the EFD [24,29,30].

Figure 9 shows the geographical map of the total electric field power integrated for the entire night-side semiorbit 2019 dataset, filtered at 19.8 kHz. The intense electromagnetic field excited by NWC transmitters can be clearly observed in both the areas above the transmitter and its geomagnetic conjugate hemisphere. The electric field response in the conjugate hemisphere is mainly evident at $L = 1.3$ – 2.5 (where L is the McIlwain parameter [31]). This feature can be explained in terms of VLF waves of NWC propagation in both ducted and non-ducted way. In fact, Kulkarni et al. [22] and Zhao et al. [24] indicate that non-ducted VLF transmitter signals can reach the opposite hemisphere very close to where a ducted signal could be reached, which means that ducted and nonducted propagation modes cannot be separated at some L-shell. The amplitude of the VLF wave is relatively smaller at the conjugate region if compared to the space region over the transmitters, due to Landau damping effect occurring when it approaches the high wave normal angle [25].

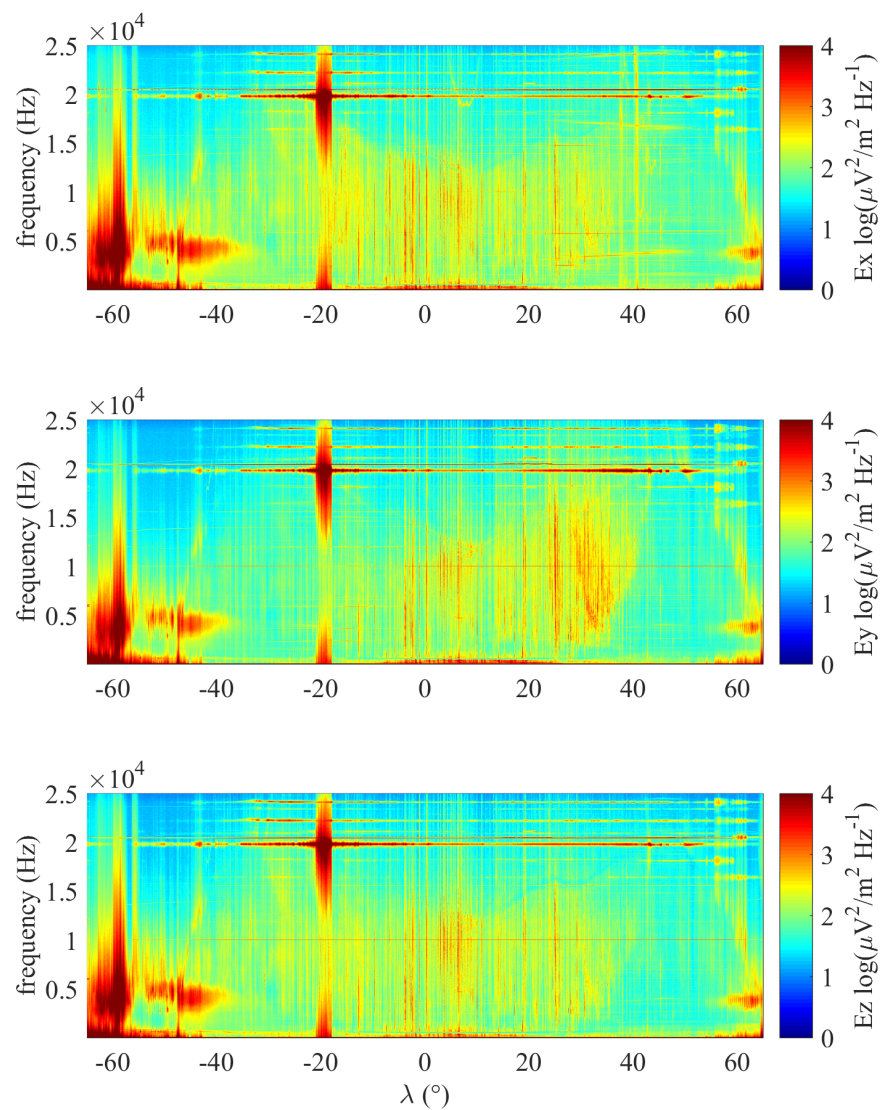


Figure 8. Spectrogram of the electric field components along the geographic North (upper panel), East (middle panel) and vertical (lower panel) directions recorded on 2 February 2019 between 18:27 UT and 19:02 UT. X-axis reports the geographic latitude.

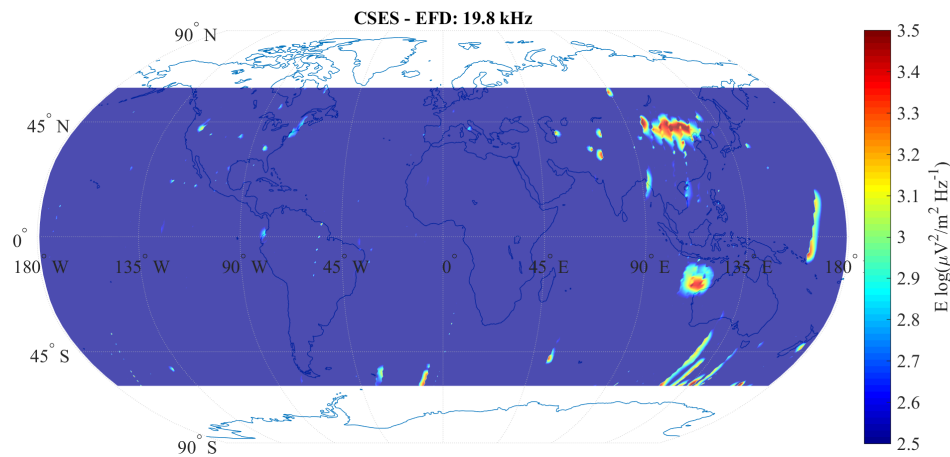


Figure 9. Geographic map showing the intensity of the total electric field recorded at 19.8 kHz by the EFD detector on board CSES-01, average value of the 2019 data. The intensity is color coded according to the color scale on the right.

4. Discussion

The comparison between the expected and measured V_f values (see Section 2) has been performed after removing the spurious effect induced by the geomagnetic field on the electric wires inside the booms ($v_s \times B$) during the satellite motion. Although the OML theory, used to compute the V_{theo} , does not take into account the effect of electric and magnetic fields, it provides reliable results until these fields do not alter significantly the isotropic electron flux due to their thermal energy. On one hand, we can consider negligible at ionospheric altitudes the magnetic field effect on the electrons collection by the probe until its radius is comparable or lower than the Larmor radius. On the other hand, the electric fields in ionospheric space can reach values capable of strongly perturbing the electron fluxes. Therefore a statistically proven separation between quiet and perturbed cases is needed. Results obtained during quiet periods of observation, with full applicability of the OML theory description, highlight the reliability of both CSES Langmuir Probes and EFD data. In fact, as shown in Figure 4, the differences between the four V_f and V_{theo} show average values lower than 1 mV. In order to better understand this result, we have to consider that EFD V_f is directly measured as a result of the true particles densities while LAP plasma density is obtained by the inversion algorithm of the electron current equation of OML theory. In the quiet case, the derived plasma density LAP values are very close to the actual ones. In fact, an hypothetical $\pm 10\%$ error in LAP plasma density detection will produce about ± 20 mV in V_{theo} . In such case, the average value of the distribution shown in Figure 4 would be about ± 20 mV as well.

A different scenario occurs when a strong electric field alters the isotropic electrons collection (i.e., OML is no longer valid) as shown in the ratios distributions in Figure 6. In such case, the expected value of V_{theo} is computed with an intrinsic uncertainty due to unknown equivalent probes collecting surface (i.e., the actual electrons flow on the probe). In this case, we can only verify that the distributions shift is in the right direction and in the predicted range as deduced by the geometrical considerations presented in Section 2.2.

Concerning the electromagnetic signals detection, EFD shows valuable capability of observing the first peaks of the ionospheric Schumann resonance quite well. In fact, though generally weak in amplitude, such waves are a common phenomenon in the CSES EFD data. Though sometimes faintly observable during the day, Schumann resonance signatures are generally detected during the nighttime. The intensity of the first peak of the electric field is $\sim 0.4 \text{ mV/Hz}^{1/2}$, about three orders of magnitude lower than typical ground based measurements e.g., References [17,32]. The difficulty to observe such a resonance during the daytime on the space-based platform can be attributed to the day-side plasma density being about one order of magnitude higher than at nighttime. Moreover, the ionospheric layer (the top of the resonant cavity) is located at lower altitude in the day-side part of CSES orbit [33]. The CSES altitude of $\sim 507 \text{ km}$ is well above the lowest altitudes of the daytime ionosphere lower layer ($\sim 90 \text{ km}$). The above factors would contribute to a dampening of the resonant wave energy reaching the satellite. Stratospheric Schumann resonance measurements gathered on-board balloons show a scale height of $\sim 25 \text{ km}$ [34], emphasizing that Schumann resonance signatures indeed decrease with altitude. In fact, they showed that at 25 km during fair weather conditions, the electric field associated to the Schumann resonance is about half of that observed on the ground despite the quiet small atmospheric conductivity in the troposphere.

Finally, in agreement with Zhao et al. [24], CSES-01 satellite clearly recorded the electromagnetic field enhancement excited by ground-based VLF transmitters. The electromagnetic field induced by NWC in the conjugate area is mainly distributed within $1.5 < L < 2.5$. The full-wave simulation reported in Zhao et al. [24] showed that the peak of the electromagnetic field basically coincides with the crossing point of the magnetic force line from the bottom of the ionosphere to the conjugate region, indicating that these VLF waves propagate in a ducted mode. The electromagnetic field of VLF signals in the conjugate area is smaller than that above the VLF transmitter because of Landau damping when the wave approaches a high wave normal angle. These results show that the nightside observation of electromagnetic field of CSES-01 satellite at VLF band is stable and reliable (Figures 8 and 9).

5. Conclusions

This paper has been written with the purpose of validating the measurements of the Electric Field Detector on-board CSES-01 satellite. For this purpose, low frequency (V_f from ULF data), medium (ELF data), and high frequency (VLF data) have been used to check the EFD capability in following the ionospheric plasma oscillations. The main results are summarized as follows:

1. Comparison between V_f and V_{theo} .
 - Quiet conditions: the results demonstrate the reliability and consistency of both CSES LAP and EFD data. In fact, the difference measured between the four V_f and the V_{theo} using the LAP density and the temperature observations (Figure 4), show average values lower than 1 mV .
 - Perturbed conditions: because of the presence of a strong electric field altering the isotropic electrons collection, the OML theory is no longer valid and thus the V_{theo} results are uncertain due to the change in the actual probes collecting surface. As a consequence, we can only verify that the distributions shift is in the right direction and in the expected range as derived by the geometrical considerations.
2. Electromagnetic signals detection capability
 - EFD shows a very good sensitivity resulting in the observation of the first peaks of the ionospheric Schumann resonance, which is a common phenomenon in the electric field data set, despite their very low amplitude.
 - CSES-01 satellite observed stable and reliable electromagnetic field enhancement excited by the NWC VLF transmitters whose peaks coincide with the crossing

point of the magnetic force line from the bottom of the ionosphere to the conjugate region. Such a phenomenon confirms the ducted mode propagation of these VLF waves.

Author Contributions: P.D. managed the manuscript and concurred in the discussion of the results; J.H. processed the CSES EFD data and concurred in the discussion of the results; M.P. made the analysis of the electric field, magnetic field and plasma data, and concurred in the discussion of the results; D.B., Z.Z., G.R., R.A., Y.-B.G., J.L., G.M., C.D.S., M.C. concurred in the discussion of the results; R.Y. processed the CSES LAP data; I.B. made the VLF data analysis; P.U. concurred in the discussion of the results; X.S. and P.P. are the Chinese and Italian PI of the CSES mission, respectively. All authors have read and agreed to the published version of the manuscript.

Funding: This research received no external funding.

Data Availability Statement: Data available in the publicly accessible repository <http://www.leos.ac.cn/>.

Acknowledgments: The authors thank both the reviewers for their comments and suggestions. The authors thank Antonio Cicone, Angelo de Santis and Livio Conti for their useful comments. This work made use of the data from CSES mission, a project funded by China National Space Administration and China Earthquake Administration in collaboration with Italian Space Agency and Istituto Nazionale di Fisica Nucleare. Mirko Piersanti thanks the Italian Space Agency for the financial support under the contract ASI "LIMADOU scienza" n° 2016-16-H0. Zeren Zhima thanks the NSFC grant 41874174 and National Key R&D Program of China (Grant 2018YFC1503501). This research was supported by the ISSI-BJ project "The electromagnetic data validation and scientific application research based on CSES satellite". This research was supported by the Dragon 5 cooperation 2020-2024 project (ID.59236).

Conflicts of Interest: Authors declare that they have no conflict of interest.

References

1. Shen, X.; Zhang, X.; Yuan, S.; Wang, L.; Cao, J.; Huang, J.; Zhu, X.; Piergiorgio, P.; Dai, J. The state-of-the-art of the China Seismo-Electromagnetic Satellite mission. *Sci. China Ser. E Technol. Sci.* **2018**, *61*, 634–642. [[CrossRef](#)]
2. Huang, J.; Lei, J.; Li, S.; Zeren, Z.; Li, C.; Zhu, X.; Yu, W. The Electric Field Detector (EFD) onboard the ZH-1 satellite and first observational results. *Earth Planet. Phys.* **2018**, *2*, 469–478. [[CrossRef](#)]
3. Diego, P.; Bertello, I.; Candidi, M.; Mura, A.; Vannaroni, G.; Badoni, D. Plasma and Fields Evaluation at the Chinese Seismo-Electromagnetic Satellite for Electric Field Detector Measurements. *IEEE Access* **2017**, *5*, 3824–3833. [[CrossRef](#)]
4. Yan, R.; Guan, Y.; Shen, X.; Huang, J.; Zhang, X.; Liu, C.; Liu, D. The Langmuir Probe Onboard CSES: Data inversion analysis method and first results. *Earth Planet. Phys.* **2018**, *2*, 1–10. [[CrossRef](#)]
5. Cheng, B.; Zhou, B.; Magnes, W.; Lammegger, R.; Pollinger, A. High precision magnetometer for geomagnetic exploration onboard of the China Seismo-Electromagnetic Satellite. *Sci. China Ser. E Technol. Sci.* **2018**, *61*, 659–668. [[CrossRef](#)]
6. Allen, J.E. Probe theory—the orbital motion approach. *Phys. Scr.* **1992**, *45*, 497–503. [[CrossRef](#)]
7. Badoni, D.; Ammendola, R.; Bertello, I.; Cipollone, P.; Conti, L.; De Santis, C.; Diego, P.; Masciantonio, G.; Picozza, P.; Sparvoli, R.; et al. A high-performance electric field detector for space missions. *Planet. Space Sci.* **2018**, *153*, 107–119. [[CrossRef](#)]
8. Piersanti, M.; Pezzopane, M.; Zhima, Z.; Diego, P.; Xiong, C.; Tozzi, R.; Pignalberi, A.; D'Angelo, G.; Battiston, R.; Huang, J.; et al. Can an impulsive variation of the solar wind plasma pressure trigger a plasma bubble? A case study based on CSES, SWARM and THEMIS data. *Adv. Space Res.* **2020**. [[CrossRef](#)]
9. Piersanti, M.; Villante, U.; Waters, C.; Coco, I. The 8 June 2000 ULF wave activity: A case study. *J. Geophys. Res. Space Phys.* **2012**, *117*. [[CrossRef](#)]
10. Piersanti, M.; Cesaroni, C.; Spogli, L.; Alberti, T. Does TEC react to a sudden impulse as a whole? The 2015 Saint Patrick's day storm event. *Adv. Space Res.* **2017**, *60*, 1807–1816. [[CrossRef](#)]
11. Vellante, M.; Piersanti, M.; Heilig, B.; Reda, J.; Del Corpo, A. Magnetospheric plasma density inferred from field line resonances: Effects of using different magnetic field models. In Proceedings of the 2014 XXXIth URSI General Assembly and Scientific Symposium (URSI GASS), Beijing, China, 16–23 August 2014; pp. 1–4.
12. Villante, U.; Piersanti, M. Analysis of geomagnetic sudden impulses at low latitudes. *J. Geophys. Res. Space Phys.* **2009**, *114*. [[CrossRef](#)]
13. Villante, U.; Di Matteo, S.; Piersanti, M. On the transmission of waves at discrete frequencies from the solar wind to the magnetosphere and ground: A case study. *J. Geophys. Res. Space Phys.* **2016**, *121*, 380–396. [[CrossRef](#)]
14. Parrot, M.; Sauvaud, J.A.; Berthelier, J.J.; Lebreton, J.P. First in-situ observations of strong ionospheric perturbations generated by a powerful VLF ground-based transmitter. *Geophys. Res. Lett.* **2007**, *34*, 11111. [[CrossRef](#)]

15. Bertello, I.; Piersanti, M.; Candidi, M.; Diego, P.; Ubertini, P. Electromagnetic field observations by the DEMETER satellite in connection with the 2009 L'Aquila earthquake. *Ann. Geophys.* **2018**, *36*, 1483–1493. [[CrossRef](#)]
16. Piersanti, M.; Materassi, M.; Battiston, R.; Carbone, V.; Cicone, A.; D'Angelo, G.; Diego, P.; Ubertini, P. Magnetospheric-Ionospheric-Lithospheric Coupling Model. 1: Observations during the 5 August 2018 Bayan Earthquake. *Remote. Sens.* **2020**, *12*, 3299. [[CrossRef](#)]
17. Nickolaenko, A.P.; Hayakawa, M. *Resonances in the Earth-Ionosphere Cavity*; Kluwer Acad: Dordrecht, Netherlands, 2002.
18. Schumann, W.O. On the free oscillations of a conducting sphere which is surrounded by an air layer and an ionosphere shell. *Z. Naturforsch. B* **1952**, *7A*, 149–154; (In German). [[CrossRef](#)]
19. Finlay, C.C.; Olsen, N.; Kotsiaros, S.; Gillet, N.; Tøffner-Clausen, L. Recent geomagnetic secular variation from Swarm and ground observatories as estimated in the CHAOS-6 geomagnetic field model. *Earth Planets Space* **2016**, *68*, 1. [[CrossRef](#)]
20. Simoes, F.; Pfaff, R.; Freudenreich, H. Satellite observations of Schumann resonances in the Earth's ionosphere. *Geophys. Res. Lett.* **2011**, *38*, L22101. [[CrossRef](#)]
21. Balsler, M.; A Wagner, C. Observations of Earth-Ionosphere Cavity Resonances. *Nat. Cell Biol.* **2006**, *188*, 638–641. [[CrossRef](#)]
22. Kulkarni, P.; Inan, U.S.; Bell, T.F.; Bortnik, J. Precipitation signatures of ground-based VLF transmitters. *J. Geophys. Res. Space Phys.* **2008**, *113*, 07214. [[CrossRef](#)]
23. Baker, D.N.; Jaynes, A.N.; Hoxie, V.C.; Thorne, R.M.; Foster, J.C.; Li, X.; Fennell, J.F.; Wygant, J.; Kanekal, S.G.; Erickson, P.J.; et al. An impenetrable barrier to ultrarelativistic electrons in the Van Allen radiation belts. *Nat. Cell Biol.* **2014**, *515*, 531–534. [[CrossRef](#)] [[PubMed](#)]
24. Zhao, S.; Zhou, C.; Shen, X.; Zhima, Z. Investigation of VLF Transmitter Signals in the Ionosphere by ZH-1 Observations and Full-Wave Simulation. *J. Geophys. Res. Space Phys.* **2019**, *124*, 4697–4709. [[CrossRef](#)]
25. Cohen, M.B.; Inan, U.S. Terrestrial VLF transmitter injection into the magnetosphere. *J. Geophys. Res. Space Phys.* **2012**, *117*, 08310. [[CrossRef](#)]
26. Parrot, M.; Inan, U.S.; Lehtinen, N.G. V-shaped VLF streaks recorded on DEMETER above powerful thunderstorms. *J. Geophys. Res.* **2008**, *113*, A10310. [[CrossRef](#)]
27. Záhlava, J.; Němec, F.; Pinçon, J.L.; Santolík, O.; Kolmašová, I.; Parrot, M. Whistler Influence on the Overall Very Low Frequency Wave Intensity in the Upper Ionosphere. *J. Geophys. Res. Space Phys.* **2018**, *123*, 5648–5660. [[CrossRef](#)]
28. Shen, X.; Zhima, Z.; Zhao, S.; Qian, G.; Ye, Q.; Ruzhin, Y. VLF radio wave anomalies associated with the 2010 Ms 7.1 Yushu earthquake. *Adv. Space Res.* **2017**, *59*, 2636–2644. [[CrossRef](#)]
29. Graf, K.L.; Spasojevic, M.; Marshall, R.A.; Lehtinen, N.G.; Foust, F.R.; Inan, U.S. Extended lateral heating of the nighttime ionosphere by ground-based VLF transmitters. *J. Geophys. Res. Space Phys.* **2013**, *118*, 7783–7797. [[CrossRef](#)]
30. Parrot, M. DEMETER observations of manmade waves that propagate in the ionosphere. *Comptes Rendus Phys.* **2018**, *19*, 1–2, 26–35. [[CrossRef](#)]
31. McIlwain, C.E. Coordinates for mapping the distribution of magnetically trapped particles. *J. Geophys. Res. Space Phys.* **1961**, *66*, 3681–3691. [[CrossRef](#)]
32. Sentman, D.D. Schumann resonances. In *Handbook of Atmospheric Electrodynamics I*, 1st ed.; Volland, H., Ed.; CRC Press: Boca Raton, FL, USA, 1995; pp. 267–298.
33. Madden, T.; Thompson, W. Low-Frequency Electromagnetic Oscillations of the Earth-Ionosphere Cavity. *Low-Freq. Electromagn. Oscil. Earth-Ionos. Cavity* **1964**, *3*, 211–254. [[CrossRef](#)]
34. Ogawa, T.; Kozai, K.; Kawamoto, H.; Yasuhara, M.; Huzita, A. Schumann resonances observed with a balloon in the stratosphere. *J. Atmospheric Terr. Phys.* **1979**, *41*, 135–142. [[CrossRef](#)]